Chapter 5

The Turbulence Regime of the Atmospheric Surface Layer in the Presence of Shallow Cold Drainage Flows: Application of Laser Scintillometry

John A. Mayfield and Gilberto J. Fochesatto

Additional information is available at the end of the chapter

http://dx.doi.org/10.5772/intechopen.80290

Abstract

The presence of shallow cold flows in the atmospheric boundary layer (ABL) instigates changes in the turbulent regime of the atmospheric surface layer (ASL). This small scale flow circulation introduces radiative cooling controls over large areas in polar latitudes during winter. In this study, microscale dynamic and turbulent variables have been obtained in the framework of the Winter Boundary Layer Experiment in Fairbanks, Alaska, developed during the winters of 2009/2010 and 2010/2011. Multiscale surface turbulence observations based on Eddy covariance and laser scintillometry were combined with Doppler acoustic sounding to document simultaneous changes in the ABL flow and ASL turbulence. We computed changes in momentum and heat fluxes characterizing intermittent and persistent modes of the drainage flow over three study cases. On the basis of laser scintillometry observations, we argue that a significant source of turbulence aiming at the surface fluxes has origins in the upper level shear-induced thermal turbulence at the top of the ABL.

Keywords: surface turbulence, optical scintillation, radiative cooling, small scale drainage flows, stable boundary layer

1. Introduction

The absence of daylight combined with snow-covered surfaces during the extreme winters in continental Alaska sets up a unique meteorological condition in the lower troposphere where surface radiative cooling becomes the dominant forcing mechanism initiating the formation of stably-stratified ABL [1, 2]. This meteorological feature is present under synoptic

anticyclone conditions (i.e., surface high pressure, clear skies) and is particularly prominent and episodic throughout the winter. In general, when this meteorological configuration sets up, several days of a persistent stably-stratified ABL occur [3–6]. This local ABL feature, also known as surface-based temperature inversion (SBI), occurs statistically over 85% of time in the presence of multiple elevated temperature inversion (EI) layers from synoptic origin [1]. In such anti-cyclone conditions and when weak horizontal synoptic flow forcing prevails, the topographic configuration and the orientation of mountains in the Interior of Alaska constrain the low-level tropospheric circulation. At the regional scale, the air flow in the ABL becomes locally quasi-laminar and regionally stagnant under strong surface radiative cooling and therefore prone to disruptions from local-scale circulation mechanisms. The investigation of this process was the objective of the Winter Boundary-Layer Experiment [7].

Mountains and hills in polar regions shelter large cold pools of air between them that are exposed to a higher radiative cooling rate than adjacent low-laying areas that may be more opened and oriented toward south (i.e., the south-sunny side). These topographic and radiative conditions set the stage for the development of density flows that takes the form of drainage flows [7]. Such small-scale flows channeled through the varying terrain morphology connect basins on the north-facing to those on the south-facing sides of the mountains and hills and profoundly affect the stability of the relatively lower and warmer basins, as well as the surface turbulent flux and momentum regime. The occurrence of these flows has been identified in other experiments on lower latitudes [8, 9] as a cold down-slope winds initiated by the temperature contrast between basins influencing therefore the strongly stratified ABL that builds up locally at the basin scale.

On the other hand, extreme winter conditions in Fairbanks, Alaska, have been known for several decades to represent a very complex air pollution problem [3, 10, 11]. Besides local anthropogenic emissions, what exacerbates the air pollution problem is precisely the naturally occurring strong surface cooling rate and, consequently, the formation of extremely low-level SBI, often complicated with multiple stratified layers [1, 2] under a stagnant flow condition. As indicated previously, these episodes are mostly present under specific synoptic conditions (e.g., calm winds and stagnant quiescent synoptic anticyclonic flows) [3, 5] over periods lasting several days [1]. Moreover, the meteorological setup, the flow configuration, and the complexity of the developed ABL structure impose stringent modeling restrictions when an accurate representation of the ABL is needed in particular for air pollution assessments [12].

The first observational study of the winter ABL in Fairbanks was carried out in mid-1970s using a bi-static sodar instrument from the National Oceanic and Atmospheric Administration, Wave Propagation Laboratory. The set of observations illustrated several dynamic aspects of the stable ABL such as propagation of waves, inertial oscillations within the ABL structure, and formation and destruction of temperature inversion and stratified layers [5, 6]. Despite of the importance of these observations in terms of improving the understanding of physical processes in the ABL and the outstanding mesoscale modeling challenges that winter high latitudes imposes no additional efforts have been dedicated to continuing these investigations until the development of Wi-BLEx [1, 2, 7]. In fact, previous studies [10, 13–15] have indicated that during the extreme winter, a heavy air mass lies close to the ground, where SBI forms

http://dx.doi.org/10.5772/intechopen.80290

as the result of a strong surface radiative cooling rate pronounced by the absence of sunlight and under a stagnant airflow often with wind speed less than ~1 ms^{-1}. In such conditions, katabatic flows have been found above the local SBI as they come down from the mountains surrounding the area. In these previous studies, and perhaps with limited observational capabilities at the time, it was also indicated that the extreme cold pool dominating the Tanana Valley air mass prevented the local SBI airflow to mix with the upper level katabatic flow. This feature is self-evident in several photographs of Fairbanks winter scenery, where a clear differentiation can be visually established when comparing tall power plant emission stacks and home heating emission systems. In this study, we provide observational evidence that during the winter period, the valley ABL is penetrated by a small-scale cold flow from the north-northwest sector of the observational site (see **Figure 1**) close to the hill slopes around Fairbanks. This shallow cold flow was observed to interact with the local ABL under specific prescribed stagnant anticyclone conditions and to dominate the thermodynamic structure and circulation of the ABL close to the foothills for specific periods of time [7]. In this case, penetrative drainage flows were observed to introduce small scale mixing, increasing thermal turbulence near the top of the ABL and re-stratification at the surface layer when the flow ceased. This flow originates upstream in sheltered cold pools of air (i.e., northern slopes of the Cranberry Hills), where the combination of geographic orientation and very low solar elevation angle during the winter allows for a more efficient radiative cooling than in the central valley region, i.e., the south facing slopes of the Tanana Valley (see **Figure 1**).

Section 2 describes the experimental setup during Wi-BLEx, and Section 3 describes the large scale meteorological conditions during the observations. Section 4 introduces the observations of drainage flows and ABL structure, and Section 5 analyzes and discusses the cases and

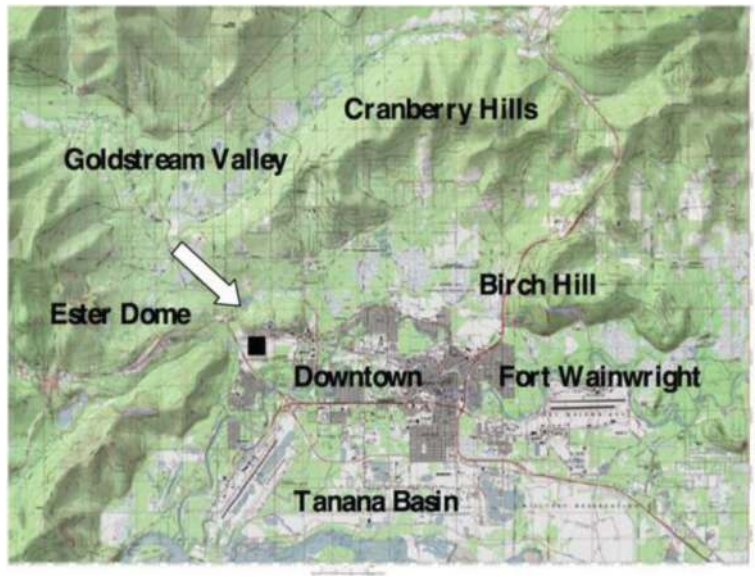

Figure 1. Topographic map of the Fairbanks area interior of Alaska. Black square indicates experimental site on the campus farm of the University of Alaska Fairbanks. The arrow indicates the direction of flow into the experimental site, where Wi-BLEx was developed. (Source: Alaska seamless USGS topographic maps).

the determination of structural and turbulent parameters of the drainage flow that influence the state of surface turbulent fluxes. This chapter concludes in Section 6 where a summary conclusion is provided based on the experimental evidence that supports the hypothesis that shear-induced thermal turbulence in the upper level depth of the drainage flow propagates downward to induce large-eddy turbulent exchanges in the ASL fluxes.

2. Experiment and methodology

Wi-BLEx took place at the University of Alaska Fairbanks (UAF) experimental farm located in the south-facing basin in the foothills of the Cranberry Hills (see **Figure 1**) on the UAF campus. The specific sets of observations discussed in this paper were carried out from November 1, 2010, to March 30, 2011, and three cases were selected for further analysis.

The instrumentation consisted of two 3D-sonic anemometers installed at 2- and 4-m height on a meteorological mast around the center of the farm (see **Figure 2**).

The sonic anemometers acquired at 10 Hz, the three components of the velocity field, as well as the sonic virtual temperature. This allows calculating turbulent quantities u′, v′, w′, and θ'. Surface-layer observations were then combined with data from an ABL profiler. In this case, an acoustic phased-array Doppler sodar (Remtech PA-0) was installed 130 m north of the sonic anemometer tower (**Figure 2**, left panel). Sodar profiles ranged from 20 to 500 m on average and were able to determine the coefficient of turbulent temperature structure parameter C_T^2, wind speed, wind direction, and vertical velocity at 10-min time intervals and 10-m vertical resolution. In order to complement the set of observations, a large aperture scintillometer (LAS) (Scintec BLS 900) was set

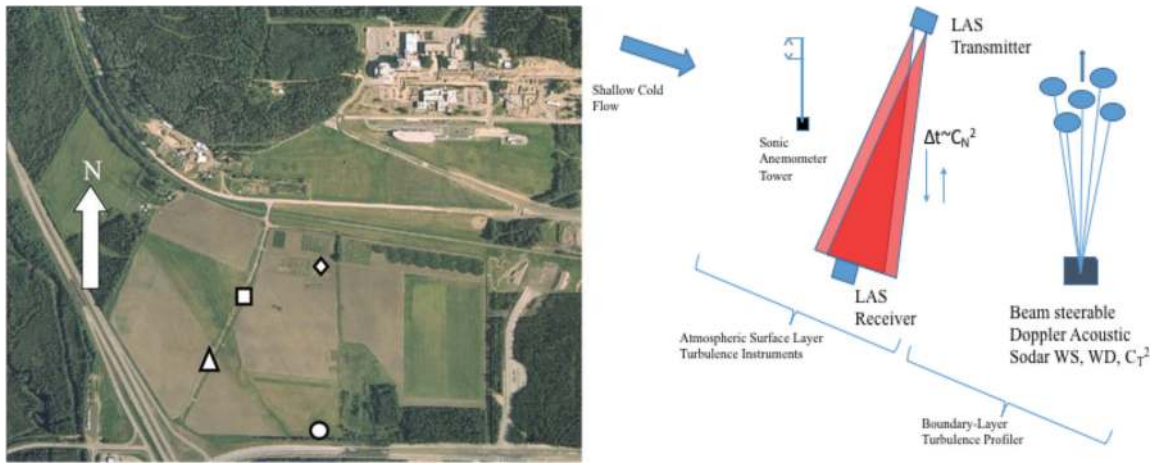

Figure 2. Aerial photo of the UAF campus farm (left panel) and conceptual idea illustrating instruments and specific observations (right panel). The site extends 1.2 km west-to-east and 700 m north-to-south. The instruments were located ~400 m from major aerodynamic perturbations upstream to the northwest caused by low-level forested area. The triangle represents the micrometeorological tower, the rhombus represents the LAS receiver, the circle is the LAS emitter, and the square is the location for the Doppler acoustic sodar. Right panel illustrate the variables and instruments applied to retrieve ASL and ABL turbulence variables (source: Photo courtesy of Alan Tonne UAF farm manager).

http://dx.doi.org/10.5772/intechopen.80290

across the basin north-south orientation to acquire the structure coefficient of refractive index turbulence C_N^2. The instrument's layout was superimposed upon an aerial photo of the UAF Campus Farm in **Figure 2** left panel, while **Figure 2** right panel shows the instrument-measurement concept. The sonic anemometers were factory calibrated before being placed in the field. Previous to the field deployment, the anemometers were installed in a closed chamber, and the acquisition electronic was calibrated for the zero-speed velocity measurement on the three components of the wind speed and temperature against the Väisälä temperature and relative humidity probe HMT-330. Similarly, the sampling rate of the sonic anemometer and the high-speed data logger were controlled for sampling rate synchronization and correct time-stamp acquisition. The methodology used to signal-process turbulent data sets from sonic anemometers and LAS follows nonlinear median filters for despiking signals [16]. And, earlier to calculating turbulent quantities, high-pass filtering techniques were applied based on the streamline coordinate rotation method [17, 18]. However, unlike the general case of turbulent flux determination in micrometeorology, the time interval to apply this methodology and preserve the turbulent fluctuations of the drainage flow events was determined to be over a window of 5 min. This time-window allows achieving the best compromise between sampling error of turbulent magnitudes and the representation of the wind measurements in terms of minimizing the probability of change in the wind direction [19]. The temperature data were processed using the same time-window interval (5 min) and using a low-pass autoregressive moving average digital filter to extract the low frequency component [20].

Based on the retrieved turbulent magnitudes, the combined auto-covariance of wind speed components and their cross-covariance allowed calculation of turbulent kinetic energy (tke) Eq. (1), surface friction velocity (u*) Eq. (2), surface momentum (τ_0) Eq. (3), and the flux Richardson number (Ri_f) Eq. (4).

$$tke = \frac{1}{2}\left[\overline{(u')^2} + \overline{(v')^2} + \overline{(w')^2}\right] \tag{1}$$

$$u^* = \left(\overline{(u'w')}^2 + \overline{(v'w')}^2\right)^{\frac{1}{4}} \tag{2}$$

$$\tau_0 = u'v' \tag{3}$$

$$Ri_f = \frac{-\frac{g}{\theta_{sfc}}\overline{w'\theta'}}{\overline{u'w'}\frac{dU}{dz} + \overline{v'w'}\frac{dU}{dz}} \tag{4}$$

$$C_N^2 = 1.22\, D^{\frac{7}{3}} d^{-3}\, \sigma_{ln(I)^2} \tag{5}$$

In Eqs. (1)–(4), θ_{sfc} is the surface potential temperature and U(z) is the wind profile and in Eq. (5), D is the diameter of the receiver's optical lens, d is the distance between emitter and receiver, while $\sigma_{ln(I)}{}^2$ is the variance of the natural logarithm of the recorded optical intensity over a given time period. The LAS emitter was operated at 125 Hz and 1 min averaging in the

receiver at 520 m distance across the basin (see **Figure 2**). The acquired data were processed to calculate C_N^2 according to Eq. (5) at 1 min time period [21]. Temperature and pressure data were acquired at approximately the center of the LAS beam and were used to estimate the heat fluxes based on Monin-Obukhov similarity hypothesis corrected by the stability functions depending of the Obukhov stability parameter (z/L) [22, 23] over a flat, snow-covered surface [24].

3. Meteorological and mean flow conditions during observations

Three cases were selected for analysis from the set of experiments carried out during Wi-BLEx. In this section, the synoptic meteorology framework and the mean flow conditions are described.

Case I (January 18–19, 2011): A surface high-pressure system was centered over the central Yukon and overtime built a surface pressure strength rising to 1040 hPa. A surface high (1043 hPa) over Siberia maintained the anticyclone motion of air masses in the interiors of Alaska. The ABL flow in Fairbanks was in stagnant condition under a weak pressure gradient force in the region, resulting in weak winds and clear skies which drove a large radiation cooling of the basins nearby the observational area. **Figure 3** illustrates the wind direction on the left panel and the wind speed on the right panel over the site. These plots are a combination of ASL and upper ABL level measured by sonic anemometer 4 m above the surface and sodar observations at 55 m and 165 m in the ABL and the free atmosphere (FA), respectively.

Case II (February 7, 2011): Observations were carried out under the influence of a surface high-pressure system that covered the Yukon and central Alaska regions (~1037 hPa surface

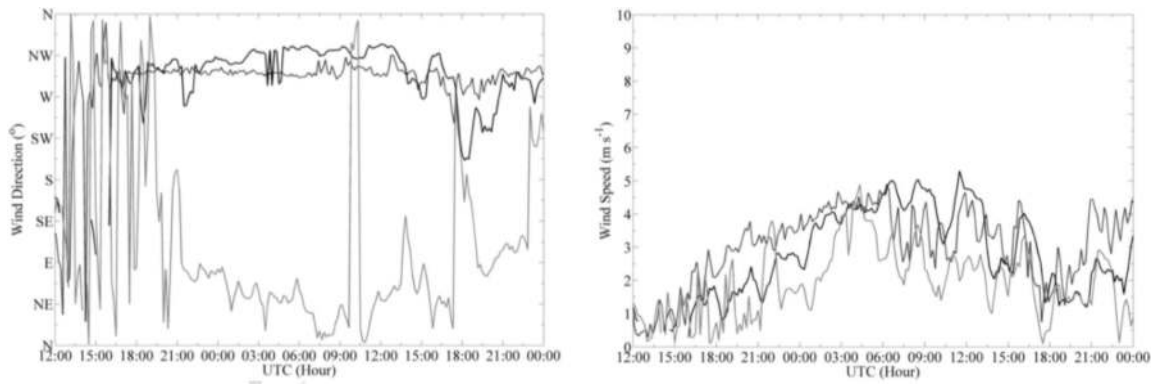

Figure 3. January 18–19 mean wind direction (left panel) and wind speed evolution (right panel) on the ASL, ABL layers, and FA. Left panel: Black solid line represents 10 min average wind direction measured by sonic anemometer 4 m height, the black dash line represents the ABL wind speed at 55 m measured by the sodar, and the gray line represents 165 m measured by the sodar. Right panel: Black solid line represents 10 min average wind speed in the ASL measured by sonic anemometer 4 m height, the black dash line represents the ABL wind speed at 55 m measured by the sodar, and the gray line represents the 165 m measured by the sodar.

http://dx.doi.org/10.5772/intechopen.80290

pressure). The pressure gradient force was weak over the Interior of Alaska, resulting in low ABL winds at the observational site. Low-level cloud coverage was suppressed by the presence of the anticyclone in the region. The surface layer flow verified the occurrence of nighttime drainage events in sequences of 270 min, followed by a drainage event of 120 min and five subsequent short-period intermittent flows in decreasing wind speed each one lasting less than 60 min. In **Figure 4**, panel on the left illustrates the wind direction and panel on the right depicts the wind speed over the site. These plots are a combination of surface 4 m height sonic anemometer 10 min averaged wind direction and wind speed and Doppler sodar in upper levels in the ABL and the FA.

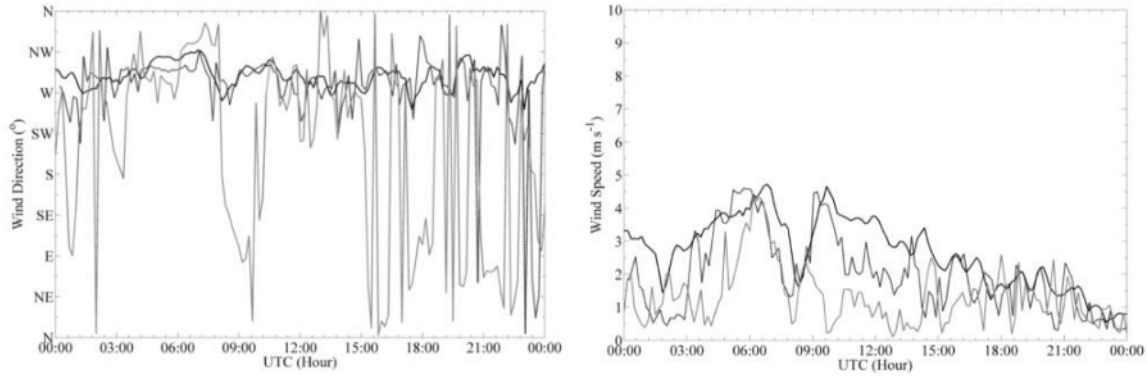

Figure 4. February 07, 2011. Left panel is the mean wind direction and right panel is the wind speed evolution in the ASL, ABL, and FA. Left panel: Black solid line represents 10 min average wind direction measured by sonic anemometer 4 m height, the black dash line represents the ABL wind speed at 55 m measured by the sodar, and the gray line represent the 165 m measured by the sodar. Right panel: Wind speed in the ASL and in the ABL layers. Black solid line represents 10 min average wind direction measured by sonic anemometer 4 m height, the black dash line represents the wind speed at 55 m measured by sodar in the ABL, and the gray line represent the 165 m measured by sodar in the FA.

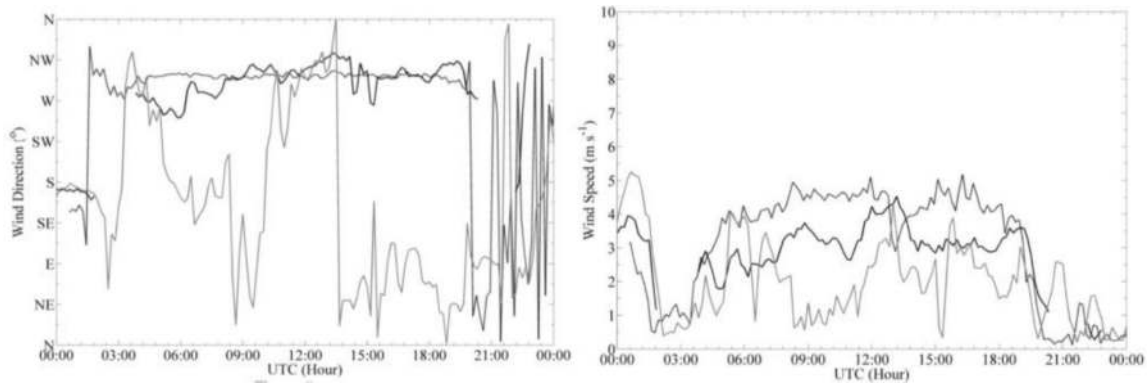

Figure 5. March 6, 2011. Left panel is the mean wind direction and right panel is the wind speed evolution in the ASL, ABL layers, and FA. In the left panel, black solid line represents 10 min average wind direction measured by sonic anemometer 4 m height, the black dash line represents the ABL wind speed at 55 m measured by the sodar, and the gray line represent the 165 m measured by the sodar. In the right panel, black solid line represents 10 min average wind speed measured by sonic anemometer 4 m height, the black dash line represents the ABL wind speed at 55 m measured by the sodar, and the gray line represents the 165 m measured by the sodar in the FA.

Case III (March 6, 2011): Observations during late winter verified the presence of a surface ridge to the south ~40 km from the observational site with tight isobars over southeast Alaska. Surface high pressure (~1036 hPa) centered over the Alaska/Yukon border established a pressure gradient force that weakened as the surface high pressure moved over the Brooks Range. The ABL state in the Tanana Valley was forced by the high pressure located around the southern Yukon and the ridge to the southwest. The winds at the geostrophic level were from the west and northwest during the night, while during the day, they were from the east-southeast. In **Figure 5**, panel on the left illustrates the wind direction and the panel on the right depicts the wind speed over the site. Similar to **Figures 3** and **4**.

4. Drainage flow events and changes in the surface turbulence

Case I: Surface wind direction observations showed a constant northwest wind direction between 15:00 UTC on 18 January and 15:00 UTC on 19 January as described in **Figure 3**. At the beginning of the event, the temperature in the atmospheric surface layer was ~−22°C and is observed to decrease in 3 h to ~−29°C as depicted in **Figure 6** left panel; vertical velocity (w) slowly increases, central panel, as the drainage flow starts to penetrate the ABL turning the surface wind direction from the northwest on the right panel and increasing surface winds.

Significant changes are observed in the surface turbulent regime obtained by auto-covariance of turbulent velocities and cross-covariances to calculate tke, u*, and τ_0. These variables are shown in **Figure 7** where in the right panel is the tke ($m^2\ s^{-2}$), central panel the increase of u*(ms^{-1}) and right panel is the momentum (m^2s^2). At the beginning, previous to the initiation of the drainage flow, the surface layer static stability was maintained to 1°C/m of stratification. During drainage flow penetration (15:00 to 21:00 UTC), the tke increased to 0.15 $m^2\ s^{-2}$, u* increased to 0.15 ms^{-1}, and τ_0 increased to 0.02 m^2s^2. The surface wind speed increased to 3.5 ms^{-1}, and the temperature dropped down by ~4°C. At 00:00 UTC, the temperature steadily decreased from −27.5°C to −30°C. When the drainage flow ceased, the surface layer re-stabilize as indicated by the calculation of the Ri_f number.

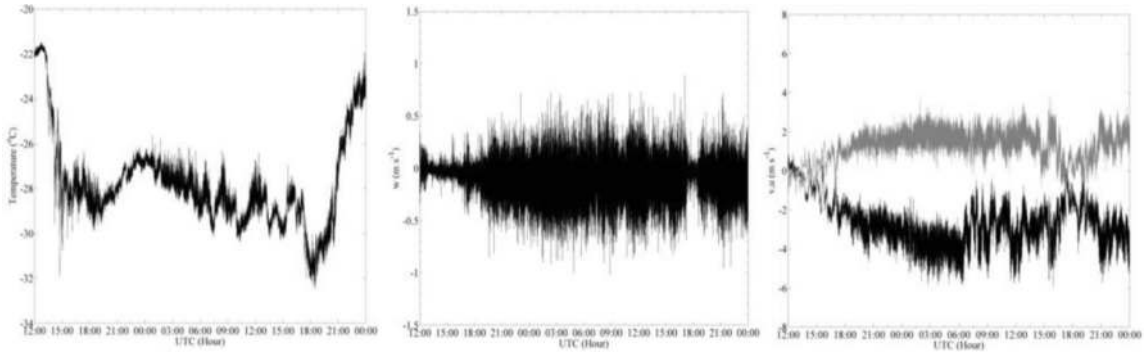

Figure 6. Turbulent variables for Case I period January 18–20, 2011, measured at 10 Hz, 4 m height sonic anemometer. Left panel represents the sonic temperature; central panel represents the vertical velocity; and right panel are the components u (black trace) and v (gray trace) of the horizontal wind speed.

http://dx.doi.org/10.5772/intechopen.80290

The vertical structure of the ABL from the 00:00 UTC 18 January shows a surface-based inversion at 108 m from the radiosonde measurements at the NWS-NOAA nearby station with winds from the south in the stable ABL and the FA [25]. This height can also be retrieved in the backscatter signature of the sodar profile by searching the point of maximum gradient indicating the decaying of thermal turbulence structure in the ABL by the C_T^2 (see **Figure 8**). Vertical and time variabilities of the C_T^2 reveal changes introduced in the ABL structure by the presence of the drainage flow on 18 January at ~15:00 UTC. The flow lasted until 19 January at 15:00 UTC. The ABL wind speed in the period from 15:00 to 22:30 UTC did not exceed 2 ms^{-1}, but in the second period from 22:30 to 17:30 UTC on 19 January, the wind speed exceeded 3 ms^{-1}. During the first period, the drainage flow was 100 m deep into the ABL, while during second period, it was shallower ~95 m. **Figure 8** displays the ABL vertical structure measured

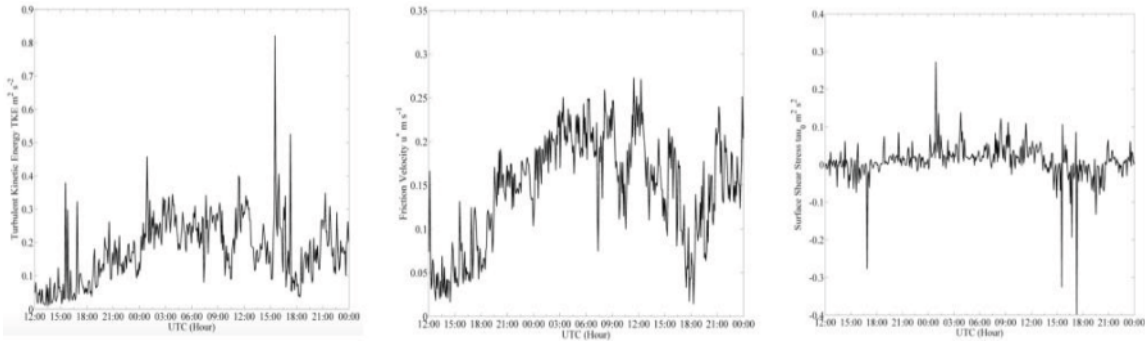

Figure 7. Case I. ASL turbulent parameters for Case I at 4 m height tke (left panel), friction velocity (central panel) and surface momentum (right panel).

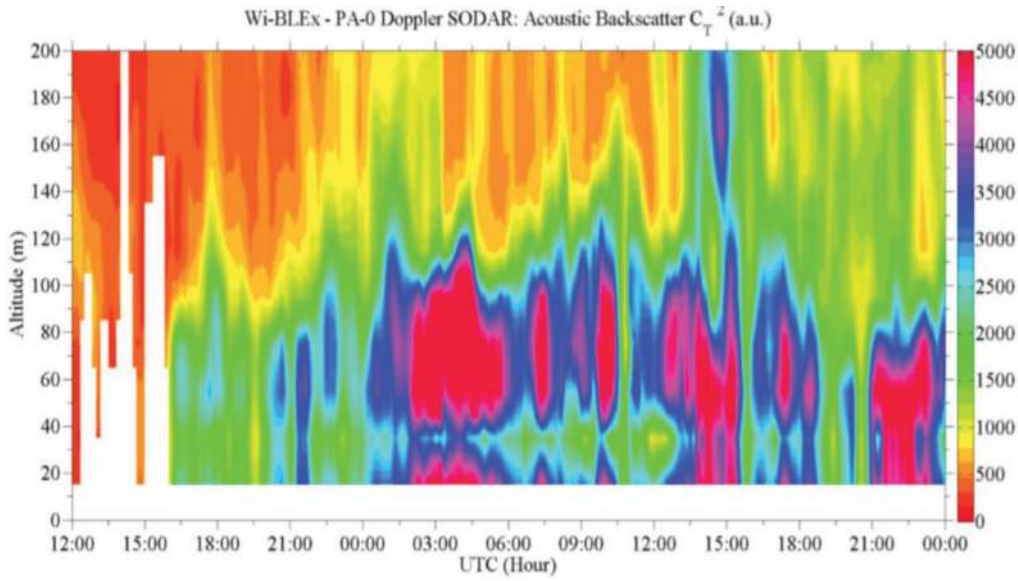

Figure 8. Case I. vertical structure of the ABL from 18 to 20 January, 2011. The sodar represents the thermal turbulent structure coefficient C_T^2 in arbitrary units with time resolution of 10 min and vertical resolution of 10 m.

by sodar, from 20 to 200 m, during the occurrence of the drainage flow. The color scale indicates an increase of the thermal turbulence C_T^2 overtime.

The C_T^2 coefficient in **Figure 8** displays a variable structure in space-time indicating increasing thermal turbulence regime as the drainage flow establishes and dominates the flow in the ABL. The ASL displays a perturbation in turbulence regime covering from surface up to ~40 m height. While this turbulence reappears after 40 m up to a range between 80 and 120 m, the spatial structures observed in the ABL responded differently to the drainage flow penetration because of the vertical stratification in the stable ABL and the increasing level of surface friction. Turbulent structures within the ABL and at the ASL overlap overtime in the period after 12:00 to 15:00 and between 21:00 and 00:00 and split for about 6 hours before 06:00 to 12:00. Remarkably, for some short periods of time, the profiler displays a complete disappearance of the thermal turbulence in the ABL for example from 19:00 to 20:00.

Case II: The beginning of this period occurred at sunset around 01:20 UTC 7 February where the initial ABL state indicated an already well-established surface-based inversion. The 00:00 UTC radiosonde from the NWS-NOAA radiosonde station PAFA showed a temperature inversion layer up to 98 m [25]. The Doppler sodar showed ABL winds from the west and FA winds from the southeast in **Figure 4**. The vertical structure measured by Doppler sodar identified a drainage flow penetrating the ABL of the basin at 4:40 UTC. The flow irruption to the basin lasted until 07:30 UTC. Wind direction observations at the surface showed an intermittent flow from northwest wind direction between 00:00 UTC on 7 February and 00:00 UTC on 8 February as described in **Figure 4**. At the beginning of the event, the temperature in the surface layer was ~−8°C and is observed to decrease in 3 h to ~−24°C as depicted in **Figure 9** (left panel), while vertical velocity (w) slowly increases **Figure 9** (central panel) as the drainage start to penetrate the ABL turning the surface wind direction from the northwest **Figure 9** (right panel). The τ_0 increased from 0 to 0.04 $m^2 s^2$, as well as the tke from 0 to 0.1 $m^2\ s^{-2}$ and u* from 0.05 to 0.2 ms^{-1}, as indicated in **Figure 10** (left, central, and right panels).

The C_T^2 profile showed a minimum at the wind maximum, while the C_T^2 maximum occurred at the wind shear layer between 90 and 110 m. The second drainage penetration event was observed by Doppler sodar between 09:10 and 11:10 UTC with a vertical structure of the

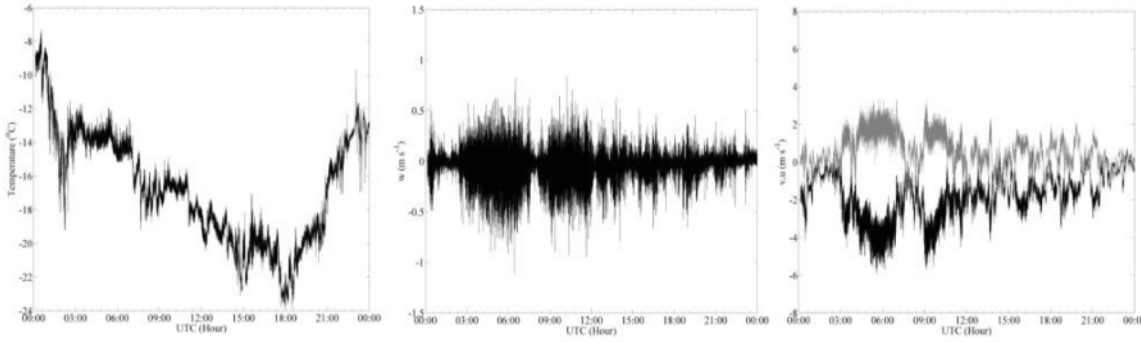

Figure 9. Case II. Turbulent variables for February 7, 2011, measured at 10 Hz, 4 m height sonic anemometer. Left panel represents the sonic temperature; central panel represents the vertical velocity; and right panel are the components u (black trace) and v (gray trace) of the horizontal wind speed.

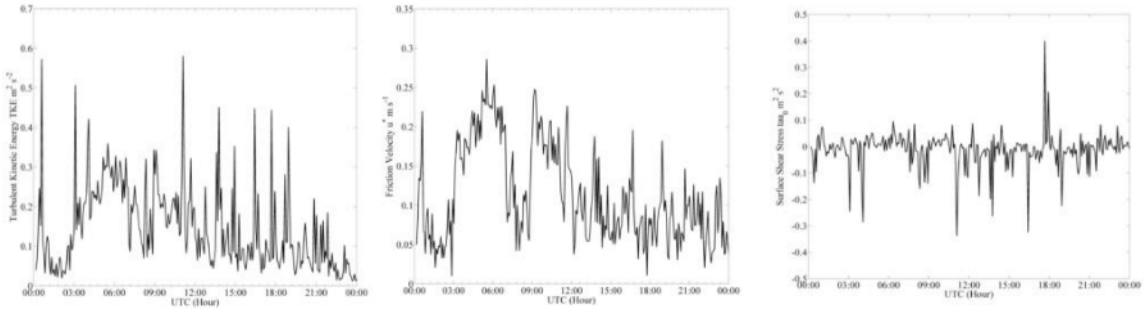

Figure 10. Case II. ASL turbulent parameters at 4 m height tke (left panel), friction velocity (central panel) and surface shear stress (right panel).

flow (i.e., wind profile) approximately similar to that of the first event. In total, this drainage episode was characterized by seven intermittent short-time duration of small scale flows. The first event lasted ~270 min. The wind speed in the surface layer was maintained at 4 ms^{-1}. This flow broke up around 07:30 UTC with a change in surface wind direction from the southwest and decreasing wind speed to less than 1 ms^{-1}. The second drainage flow event occurred from 09:00 to 12:00 UTC. The first half of this period sustained a surface wind speed that reached 4 ms^{-1}, but wind speed decreased to 2 ms^{-1} during the second half of this event. Similarly, τ_0 increased from approximately 0 to 0.03 m^2s^2, the tke increased to ~0.03 $m^2\ s^{-2}$, and u* increased to 0.02 ms^{-1}. The five remaining events lasted less than 30 min developing surface wind speed less than 2 ms^{-1}. Calculation of surface turbulent magnitudes retrieved similar behavior as compared to Case I, despite this case is composed by short bursts of sub-mesoscale flows. During the five intermittent pulses in the latter half of the day, strong stratification aloft occurred, indicated by the vertical C_T^2 in **Figure 11**. **Figure 10** shows the changes in the surface turbulence parameters, tke increased to 0.1 $m^2\ s^{-2}$, and momentum increased to 0.03 m^2s^2. The vertical structure of the ABL (see **Figure 11**) increases in C_T^2 as result of the increasing temperature variations. In the upper ABL levels, the drainage flow introduces localized levels of turbulence bounded by stratify layers from 75 m in 125 min with similar behavior in five other intermittent pulses that occurred with wind speed less than 2 ms^{-1} at 13:30, 15:20, 16:20, 19:10, and 20:30 UTC. The Doppler sodar shows evidence of the drainage pulse with an increase in horizontal wind speed and increased and localized C_T^2 values from 20 to 120 m.

Case III: In this case, the sunset on the March 6, 2011 occurred at 03:20 UTC and the surface layer was in near-neutral state; flows in the FA were from the south-southeast, and wind speeds at the 400 to 500 m level exceeded 8 ms^{-1}. The surface temperature was −9.5°C, and the surface stratification reached 3°C between the two sonic anemometer levels (see **Figure 12**). The ABL begin a rapid stratification after ceasing solar radiation input, giving rise to a rapid radiative cooling at the surface and air layers aloft. The drainage flow penetrated the ASL with the early nocturnal inversion in the time interval from 03:40 to 03:50 UTC. Surface winds turned to the northwest direction between 06:10 to 06:20 UTC. Later on, the surface winds displayed a northwest to west-northwest wind direction between 04:30 and 19:30 UTC. When the flow events ceased, the static stability buildup immediately as the wind speed slowed down to less than 1 ms^{-1} at the surface and tke, u*, and τ_0 dropped to very low values as shown in **Figure 13**.

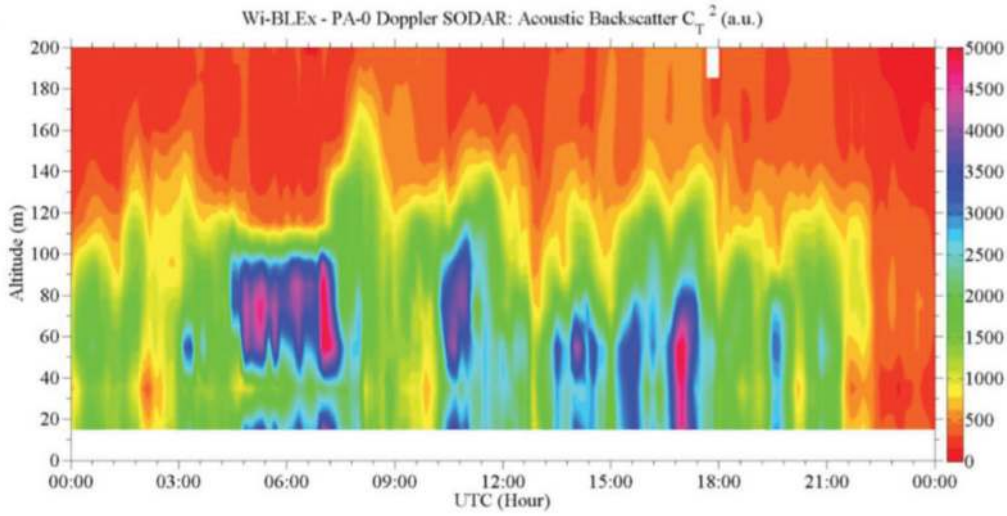

Figure 11. Case II. Vertical structure of the ABL during February 7, 2011, represented by the thermal turbulent structure coefficient C_T^2 in arbitrary units with time resolution of 10 min and vertical resolution of 10 m.

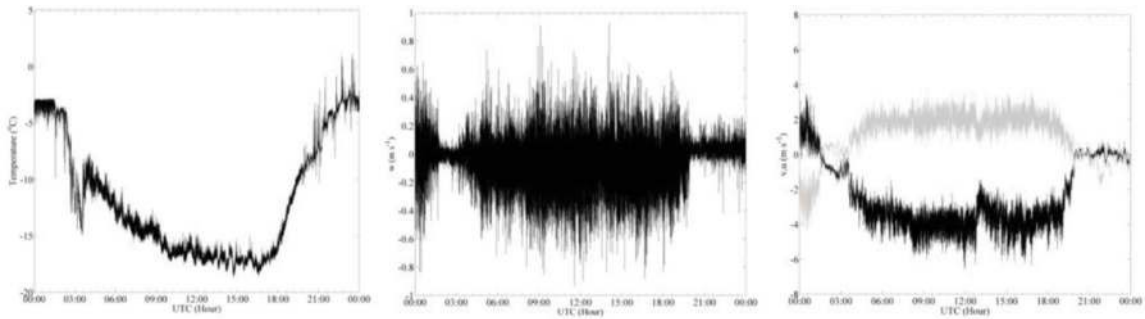

Figure 12. Case III. ASL turbulent flow measured at 10 Hz, 4-m height sonic anemometer during March 6, 2011. Left panel is the sonic temperature. Central panel is the vertical velocity and right panel are the components u (black trace) and v (gray trace) of the horizontal wind speed.

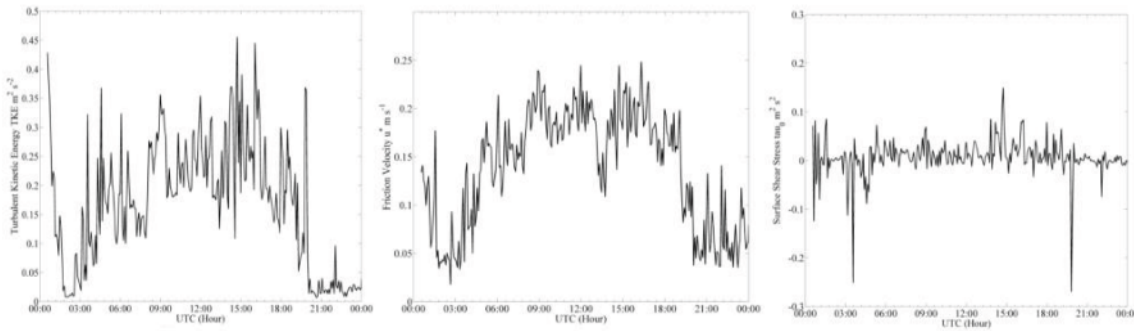

Figure 13. Case III. ASL turbulent parameters at 4 m. Left panel represents tke, central panel represents friction velocity, and right panel is the surface momentum.

During this period of time, the surface layer was in a transitional period until the vertical cooling initiated the formation of a stable ABL. As the initial drainage flow from the northwest direction penetrated the surface layer, the tke increased from ~0 to 0.2 $m^2 s^{-2}$, u_* increased from ~0.05 to 0.2 ms^{-1}, and τ_0 increased from ~0 to 0.03 $m^2 s^{-2}$, while the temperature decreased from −3°C to −18°C, a drop in about 15°C in ~15 h.

The Ri_f calculated was highly variable taking negative and positive values before the onset of the drainage flow. Ri_f decreased and reached a steady value above 1 corresponding to a quasi-laminar flow. The end of the disruptive flow was indicated by the change of wind direction to the southeast and a reduction in the wind speed and the surface micrometeorological variables tke, u*, and τ_0 at 20:00 UTC. The sun rose at 16:21 UTC, and the surface-layer temperature began to rise at 17:00 UTC. The most active turbulent activity was verified to occur between 09:00 and 15:00 UTC, when the surface parameters were at their maximum dynamic swing and wind speed was sustained overtime, while the Ri_f number indicates a dynamic unstable flow. The vertical ABL structure observed by Doppler sodar indicates increasing C_T^2 values as shown in **Figure 14** from 09:00 to 15:00 UTC when, at the same time, the wind speed was accelerating in the vertical. The C_T^2 within the region decreased suddenly in the layer from 50 to 100 m, while at the surface, high fluctuations occurred in the Ri_f number and τ_0, and the wind speed decreased (see **Figure 5**). The flow re-stabilized afterward and became dynamically stable with Ri_f number ~2. After 18:00 UTC, the Ri_f number variability increased as the flow stability broke down. The vertical profile of C_T^2 fluctuated at higher values during the transition of change in wind direction followed by an increased stratification in the basin. Of note here, **Figure 12** (central panel) illustrates a significant drop in the turbulent vertical velocity.

The vertical C_T^2 structure of the stable ABL assumed a characteristic pronounced parabolic shape up to the top of the stable ABL when the drainage penetrates. The C_T^2 profiles obtained from the Doppler sodar show a particular structure, with higher values in the vertical range from 20 to 60 m and a minimum at the drainage flow wind speed maximum. A second maximum produced the strongest signal in the acoustic echo and represents a shear layer at 100-m height. The depth of the drainage flow varied between 80 and 120 m depth. This shear layer induced thermal turbulence and entrainment of air into the ABL. In the time interval between 09:00 and 15:00 UTC, the drainage flow wind speed accelerated from 3 to 5 ms^{-1} with an increase of the C_T^2, reaching a maximum peak wind speed of 6 ms^{-1}. Between 18:00 and 21:00 UTC, the flow decelerated from 5 ms^{-1} with an increase C_T^2 (See **Figure 14**).

Summarizing, records of the ABL vertical structure obtained from Doppler sodar observations in **Figures 8** and **11–14** indicate the presence of localized turbulence in upper levels of the ABL when the drainage flow is present in the basin; in this case represented by an increases of C_T^2. Scrutinizing further the data sets obtained by Doppler sodar (i.e., wind speed and wind direction), it was verified that this turbulence appears to be induced by shear mechanism on layers along the side of the drainage flow. Similar to results from [26–28] who relates the sodar scattering cross-section to vertical potential temperature gradient and wind shear, [29] and [28] showed an echogram facsimile in which drainage flow velocity and the echo intensity increases. Nevertheless, in polar atmospheres during winter, this signature unequivocally represents shear instead of convective plume development. This differentiation was

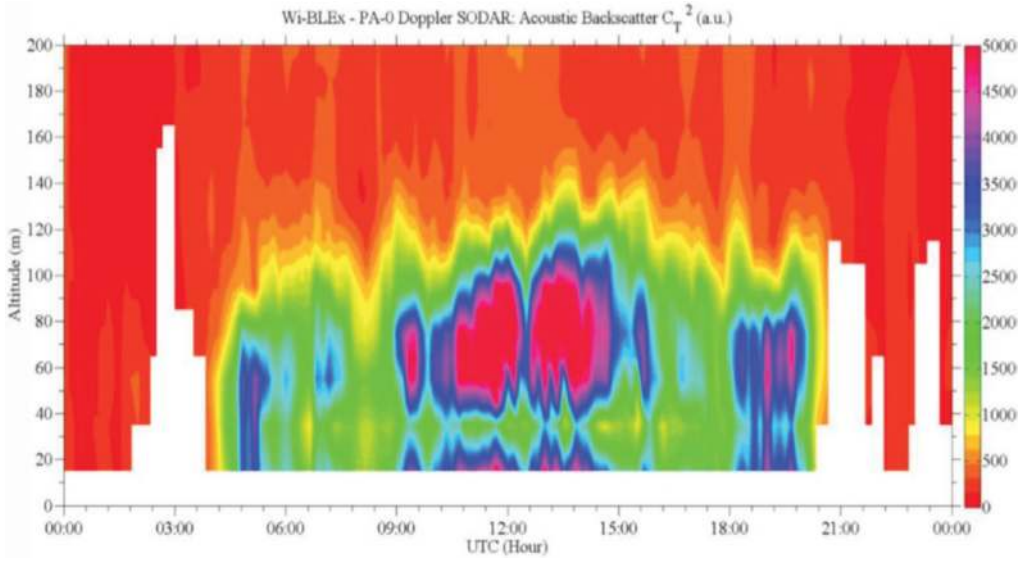

Figure 14. Case III. Vertical structure of the ABL from 6 March sodar represented by the thermal turbulent structure coefficient C_T^2 in arbitrary units with time resolution of 10 min and vertical resolution of 10 m.

illustrated for very different atmospheric and surface conditions by [30]. In this early study, the signature of acoustic backscattering in the presence of drainage flow and shear driven by convective plumes that arise from surface heating was clearly demonstrated.

5. Discussion

The turbulent state of the ASL was observed to significantly change in the presence of the shallow cold drainage flow into the basin. After scrutinizing all recorded cases during Wi-BLEx, it was found that this flow develops based on two modes: persistent flow represented by Case I and III and intermittent flow represented by Case II. Changes in the turbulence regime of the ASL, instigated by the penetration of the drainage flow into the basin's ABL, have been determined by means of two instruments sonic anemometer and LAS. These two instruments sample basically the same turbulence spectrum with the difference that sonic anemometers are in-situ sensors, while LASs are large-scale area-average turbulence sensing devices. Both instruments respond to the turbulence developed by the flow upstream on overlapping footprints. However, in this experiment, the LAS was installed across the basin (see **Figure 2**) to continuously evaluate the turbulent state of the drainage flow in space and time and thus fully record the turbulent structures developing from microscale to basin scale.

Based on Monin-Obukhov similarity hypothesis, the sensible heat flux was calculated for both instruments LAS (H_{LAS}) and sonic anemometer as indicated previously using 5-min intervals eddy-covariance integration (H_{EC}) [23, 24]. The H_{LAS} was calculated using friction velocity (u*) and the Obukhov length (L) obtained based on sonic anemometers measurements. The LAS covered an optical path length of 520 m across the basin. In this case, H_{EC} was proven to capture

http://dx.doi.org/10.5772/intechopen.80290

in the range of 70–80% up to 100% of the surface turbulent fluxes developing at the basin scale when compared to H_{LAS} [7]. This result, indicating a divergence between the calculated heat fluxes over certain time periods, pointed to the idea that large-eddy turbulence could be present in the ASL [31, 32]. On the other hand, it can be argued that given the variability of the flow in the ASL, a time variable integration is needed to account for the entire eddy flux for the case of H_{EC}. Nevertheless, the nature and source of the large eddies present in the basin can be independently investigated. These eddies can be either part of the natural mode by which the drainage flow develops breaking up the stratification in the basin (i.e., by carrying large eddy momentum) or they can be eventually part of the turbulence generated at the ABL level that would breakdown and dissipate at the surface. To further speculate on the nature of the large-eddy inducing optical turbulence in the LAS system, **Figure 15** conceptualizes the turbulent transfer mechanism supporting the argument that shear-induced turbulence along the side of the drainage flow enhances C_T^2 in the ABL and propagates down to the surface as seen by LAS.

Therefore, in what follows we analyze, each study case based on LAS optical scintillation times series and the calculated spectrogram. This analysis is guided by the flow dynamic and turbulence (i.e., wind direction, speed, and the C_T^2) register by Doppler sodar and sonic anemometers (section 3 and 4). In this case, the use of surface and ABL profiler allows determining the time interval when the drainage flow breaks into the basin and also evaluates the intervals when large eddies are present in the surface due to turbulence in ABL levels.

In the analysis of Case I, it was noted that between 15:00 and 00:00 UTC of the following day, at the initiation of the drainage flow, H_{EC} on average is ~−4 Wm^{-2}, while H_{LAS} is ~−8 Wm^{-2} without major flux differences. However, in the period from 00:00 to 09:00 UTC, the time averaged turbulent flux values are H_{LAS} −18 Wm^{-2} and H_{EC} −14 Wm^{-2}, showing an increasing divergence between the measurements. This discrepancy is consistent with the increasing probability of wind direction change thus affecting the H_{EC} measurements. Because of the dynamic changes in the flow, the H_{EC} and H_{LAS} measurements are therefore not convergent during this period (see **Figures 3** and **6**).

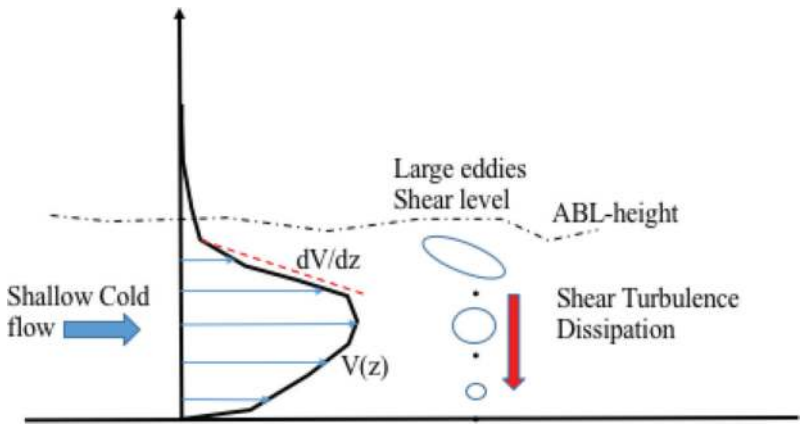

Figure 15. Conceptual scheme describing the mechanism for shear induced turbulence in the presence of a shallow cold flow. Upper ABL level illustrates wind speed shear that breaks down propagating and dissipating toward the surface. These localized large eddies impact the optical turbulence signature of LAS.

The time-series of C_N^2 exhibits large excursions in the order of ~2 to 4.10^{-13} ($m^{-2/3}$) mainly at the beginning and at the end of the study case from 12:00 to 18:00 January 18 and after 18:00 on January 19. This time variability can be seen in **Figure 16** top panel. However, during the time period where the flow in the basin establishes and fully develops, as depicted in **Figures 3** and **6**, the optical turbulence of refractive index verifies a steady increase in the signal level. This smooth increase in turbulence level corresponds to the signature described in **Figure 4**, where an increase in the turbulent intensity in w' is verified. Mostly as the flow establishes and increases speed, it also develops high-frequency turbulence as depicted in **Figure 6** which in turn also develops further tke and u*. However, the time series of C_N^2 (**Figure 16** top panel) also verifies sudden signal increases lasting longer time periods basically from ~ 10 min to more than 1 h between 18:00 and 15:00 UTC of the following day. Therefore, in order to analyze the observed variability in C_N^2 in terms of time-frequency contribution to the turbulence spectrum and confirm the existence of localized low-frequency turbulence, a multiresolution analysis based on continuous wavelet transform was conducted as depicted in **Figure 16** bottom panel. Scrutinizing this spectrogram in more detail, a sustained level of turbulence is shown to appear fluctuating overtime on periods going from 32 min. to less than 256 min. During this period of time, the flow is established in the basin given the levels of wind speed, preserved wind direction, raise of u* and tke, and therefore one of the sources for large eddies could be the localized turbulence appearing in the ABL's upper levels as illustrated by Doppler sodar in **Figure 8**. This dynamic connection is facilitated by the fact that the ASL stratification has been erased by the drainage flow penetration. This spectrogram also clearly depicts the existence of large-eddies in the basin at the beginning of the drainage flow period 12:00 to 18:00 and when the flow ceased to occur after 18:00. However, in these two time periods, the source of large eddy turbulence is basically the flow momentum transport and its horizontal variability. In fact, during these two periods of time, the flow in the basin meanders and in the first case by gaining momentum breaks the stratification propagating large eddies in the basin, while in the second period, the flow ceases meandering carrying less-energetic large eddies.

For Case II on 7 February 2011, LAS was not working for about 30 min. after 21:00 UTC. Thus, in order to provide a continuous spectral analysis, the signal was cut-off at 21:00 UTC as seen in **Figure 17** both panels. In this case, the average H_{LAS} and H_{EC} reached values of ~ −20 Wm^{-2} with the first sustained drainage flow pulse, while the second intermittent flow pulse developed an H_{LAS} and H_{EC} on average ~−16 Wm^{-2}. The wind speed in the two intermittent pulses changes rapidly over a short period of time, and eddy covariance was calculated over 5 min. integration period as indicated previously. LAS and EC flux measurements compared well in time. Similarly, to the analysis of Case I, the time series of C_N^2 exhibits periods of time with strong turbulent development reaching values of 4.10^{-13} $m^{-2/3}$ signal with a much higher time variability and sustained turbulence levels for periods of hours (**Figure 17**, top panel). This time variability in the surface turbulence is given by the flow intermittency that manifests on burst of C_N^2 lasting a couple of hours. The spectrogram in **Figure 16** (bottom panel) exhibits several periods in which spectral deposition of turbulence is verified at time scales from 16 to 256 min due to the presence of large eddies aiming the flow in the basin. This spectral patchiness correlates in some cases with localized turbulence occurring in upper shear layers of the ABL as demonstrated by localized enhancements of C_T^2 (see **Figure 11**). However, unlike Case I, the

http://dx.doi.org/10.5772/intechopen.80290

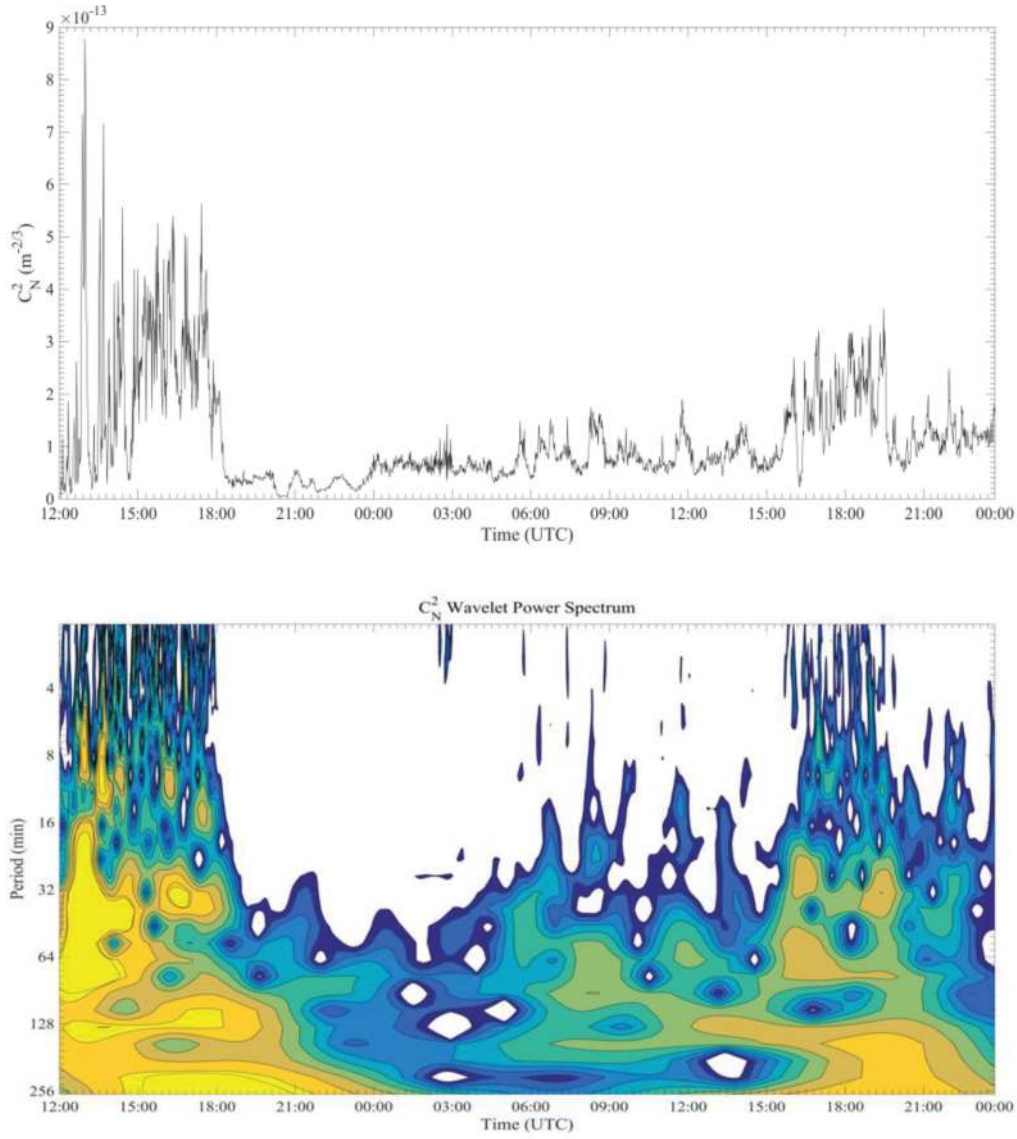

Figure 16. Case I. Turbulence of refractive index C_N^2 (m$^{-2/3}$) obtained by LAS. Top panel is the time series of 1 min time integration at 125-Hz laser pulse repetition frequency. Bottom panel is the multiresolution Morlet wavelet spectrogram.

flow is interrupted by introduction of eddies at the period scale of 16–64 min and in response to changes in signal aloft evidenced by C_T^2 in **Figure 11** that shows localized turbulence on shorter time scales than previous Case I. This sequence of flow events resulted in overall negative heat flux excursions ranging from −20 to −40 Wm^{-2} during the first pulse and from −10 to −20 Wm^{-2} in the second event. The spectral feature on the scale of 16–64 min shows turbulence in the flow that could be originated by a combination of variable longitudinal scales aiming the drainage flow and vertical coupling to the ABL where localized shear turbulence of C_T^2 breaks down propagating to the surface. As indicated earlier, each time the drainage flows disrupted the basin, large eddies aiming the flow momentum break through the stratification of the

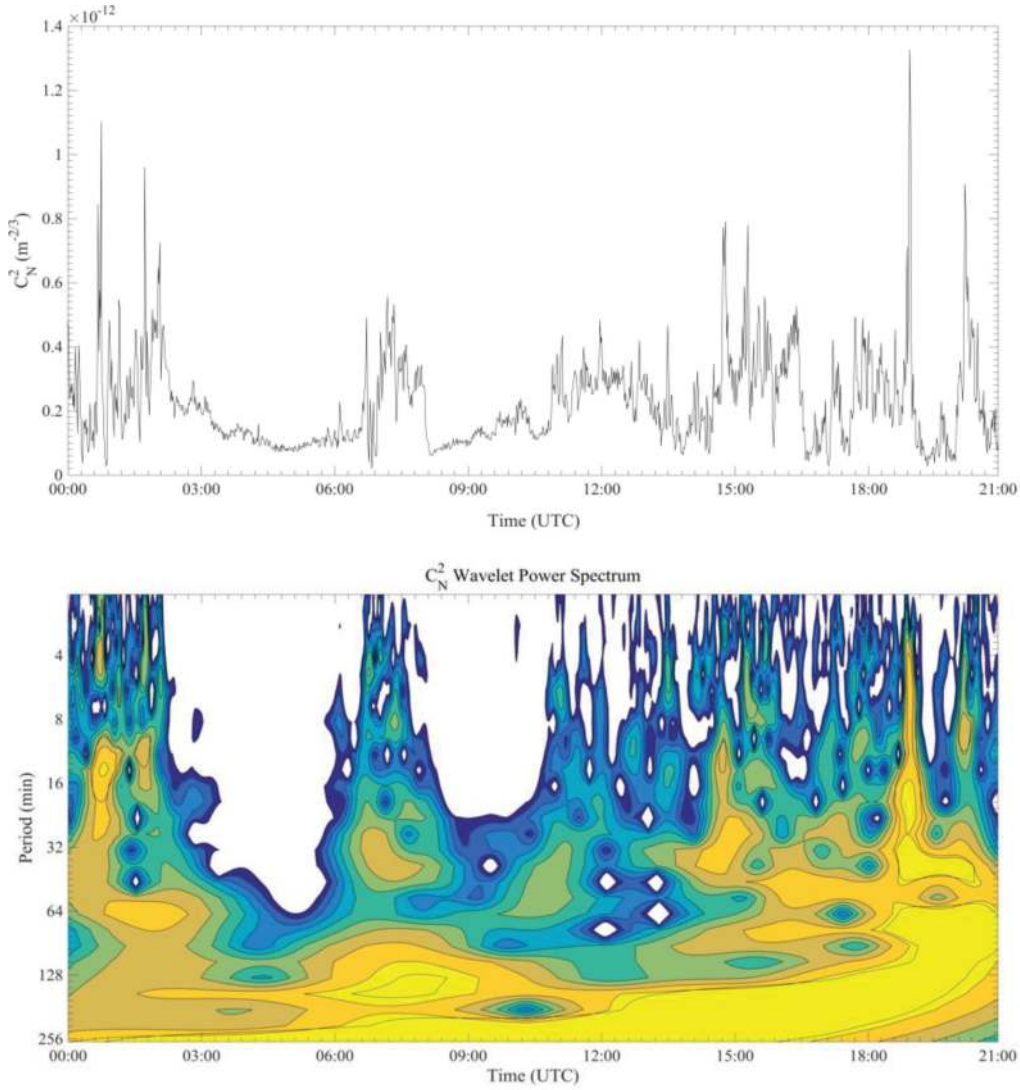

Figure 17. Case II: Turbulence of refractive index C_T^2 ($m^{-2/3}$) obtained by LAS. Top panel is the time series of 1-min time integration at 125-Hz laser pulse repetition frequency. Bottom panel is the multiresolution Morlet wavelet spectrogram.

basin, enabling vertical mixing and therefore allowing cascading turbulence from deep shear layers ~120 m (see **Figure 11**) propagating down to the surface (**Figure 15**).

Finally, for Case III, computed fluxes based on H_{LAS} and H_{EC} diverge in the presence of the drainage flow. For this period, the average values of H_{EC} and H_{LAS} are −20 and −40 Wm^{-2}, respectively. H_{LAS} is systematically higher than H_{EC} throughout the period (03:00 to 18:00 UTC), and this difference is larger than the statistical fluctuation and random errors in EC methodology. The drainage flow enters the basin in the period of time from 9:00 to 15:00, and both H_{LAS} and H_{EC} measurements peak to similar values. The time series of C_N^2 in **Figure 18** top panel displays a large variation in the turbulence of refractive index at the beginning of the drainage flow (00:00 to 4:00 UTC) and at the end when the flow ceased in the period (18:00 to 21:00 UTC).

http://dx.doi.org/10.5772/intechopen.80290

While the drainage flow is present in the basin, the general trend in C_N^2 is to reduce intensity of turbulence as high-frequency eddies aim the ASL turbulent regime with some fluctuation in the order of 20 min, which explain the difference observed in the heat flux comparison. However, analyzing the vertical structure of the flow, it can be verified that the wind profile experiences shear in layers from 20 to 40 m and at 80 to 160 m. In this case, the periodogram in **Figure 18** bottom panel shows little activity for long periods as the drainage flow evolves in the basin with the exception of two instances when the drainage flow develops localized turbulence in upper levels before 12:00 and between 12:00 and 15:00 UTC, approximately. In these two occasions, it is seen a deposition of turbulent energy in the spectrum on the ~32 min period coincidental with the occurrence of localized upper level ABL C_T^2 turbulence (see **Figure 14**).

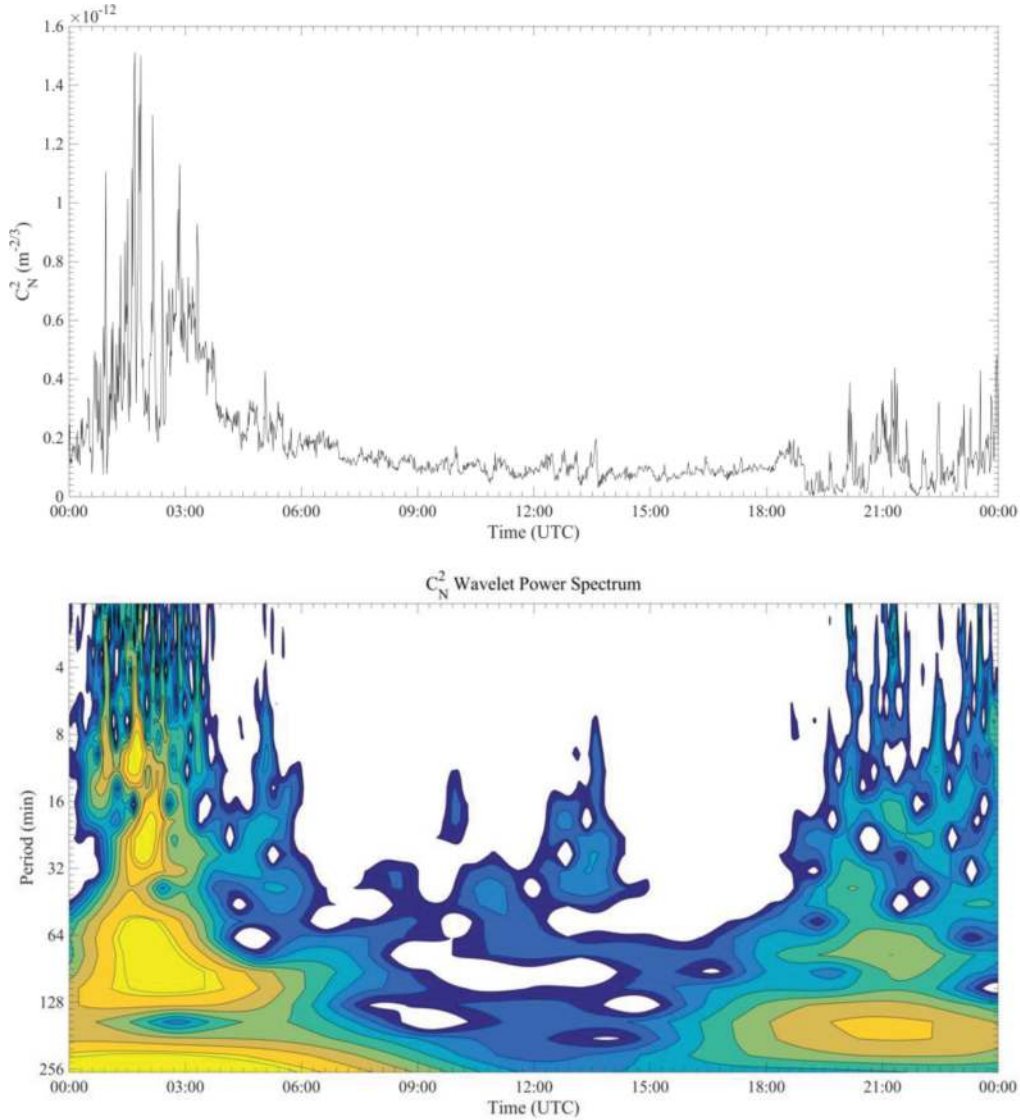

Figure 18. Case III: Turbulence of refractive index obtained C_N^2 by LAS. Top panel is the time series of 1 min time integration at 125 Hz laser pulse repetition frequency. Bottom panel is the multiresolution Morlet wavelet spectrogram.

6. Conclusions

As a summary, this chapter presents an analysis of atmospheric turbulence based on field experiments including instruments for the ASL and the ABL. The objective of Wi-BLEx was to provide a new data set illustrating the dynamic and turbulence regime of a small scale flow penetrating a high latitude basin during extreme winter conditions. The study focuses on quantifying the temporal and spatial aspects of the developing turbulent structures in the ABL and in the ASL and their possible interaction in the conditions high-latitude polar atmospheres. Data sets from Wi-BLEx observations clearly demonstrate the influence of shallow cold drainage flows in the surface turbulent fluxes and the occurrence of large-eddy spectral structures of turbulence during winters in polar regions. Of particular importance in this experiment is the use of high-frequency optical scintillometer to determine the presence of large-eddy turbulence in the ASL that would have been difficult to resolve by sonic anemometers alone in particular when nonstationary flows are under analysis [32].

In this work, three cases were selected for analysis and discussion. The selected cases develop different temporal behavior, surface signatures, and turbulence patterns throughout the vertical structure of the ABL. Of special interest here is the notion that a small scale shallow cold flow entering the basin introduces surface mixing and localized areas of turbulence within the vertical structure of the ABL. Moreover, based on tower observations, it was verified that after drainage flow ceased, the surface layer rapidly re-stratifies in response to the outstanding radiation cooling rate of winter polar atmospheres. In all cases, the drainage flow observed in the vertical by Doppler sodar is represented by wind speed profile that has been observed previously under similar flow dimensions [9, 30, 33].

It is important to note that during winter, the absence of shortwave incoming radiation sets the surface radiation budget to low levels in absolute terms and mostly depending on longwave net radiation. Therefore, heat fluxes resulting from small scale dynamic processes are limited in absolute values up to 20–30 Wm^{-2} with episodic events of 40 Wm^{-2}.

The cooling effectiveness of the drainage flow was the stronger in the intermittent Case II from all cases but only for short periods of time. A temperature drop of 11° C was verified with an average heat flux of −40 Wm^{-2} during the first intermittent pulse, while the rest of the intermittent events exhibited a lower negative average heat flux in the range of −10 and −5 Wm^{-2}.

In conclusion, during winter, the interaction between polar atmospheres and landscapes combined with the presence of specific synoptic meteorological configurations clearly evidence the possibility of an inter-valley density flow impacting the surface energy balance at a regional scale. This mechanism was evident in the three analyzed cases but also throughout the Wi-BLEx data sets.

Large scale synoptic flows play an important role at regional level to onset the occurrence of drainage flow. Based on the analyzed information, the mode in which the drainage flows develop sustained or intermittent has a combined synoptic and topographic dependence. However, the spatial and temporal scales of the resulting drainage flow depend upon the actual flow-basin dynamic, turbulent, and radiative conditions.

All cases occurred under a surface high pressure forcing in the region. This synoptic meteorological feature is important because it normally comes with a weak pressure gradient force characterized therefore by weak horizontal winds and clear skies, strongly driving the radiative cooling in the basin. During the late winter, Case III, because of the diurnal effect of solar radiation, the study fundamentally differs from the central-winter cases I and II. The drainage event under analysis developed during the night of March 5, 2011 and the day of March 6, 2011. The flow dynamic setting for this case resembles the cases collected during Wi-BLEx during the late winter, in particular for the period March 1 to 10, 2011.

Finally, the three cases described in this study can be summarized as: Case I characterized by a sustained flow lasting ~18 h in the central part of the winter; Case II is characterized by intermittent flow pulses occurred lasting less than ~3 h in the central part of the winter; and Case III resulted a sustained flow lasting for about 9.5 h in late winter. Altogether surface and vertical observations demonstrated that localized turbulence in the ABL depth, as measured in the terms of C_T^2, resulted from an increased flow speed in the ABL that impacted the ASL turbulent regime. In fact, large-eddy dynamic during the flow irruption introduced mixing in the ASL erasing stratification and enabling downward propagation of shear induced thermal turbulence in the ABL to down to the ASL. This is demonstrated by an enhancement of turbulence energy deposition in the low frequency range measured by optical scintillometry.

Acknowledgements

Wi-BLEx was supported by the Air Quality Office of the Fairbanks North Star Borough and by funding from the Department of Environmental Conservation of Alaska. Instrumental support is also recognized from the US Eielson Air Force Base in Alaska. During the Wi-BLEx observational field campaign, both authors were supported by the Geophysical Institute and the College of Natural Science and Mathematics of the University of Alaska Fairbanks. Support for the Chapter Book publication was granted form the Office of the Science of the Vice-Chancellor for Research Prof. Larry Hinzman, University of Alaska Fairbanks.

Conflict of Interest

The authors declare no conflict of interest.

Author details

John A. Mayfield and Gilberto J. Fochesatto*

*Address all correspondence to: gjfochesatto@alaska.edu

Department of Atmospheric Sciences, Geophysical Institute and College of Natural Science and Mathematics, University of Alaska Fairbanks, Fairbanks, Alaska, USA

References

[1] Mayfield JA, Fochesatto GJ. The layered structure of the winter atmospheric boundary layer in the interior of Alaska. Journal of Applied Meteorology and Climatology. 2013;**52**:953-973

[2] Malingowski J, Atkinson D, Fochesatto GJ, Cherry J, Stevens E. An observational study of radiation temperature inversions in Fairbanks, Alaska. Polar Science. 2014;**8**(1):24-39

[3] Bowling SA, Ohtake T, Benson CS. Winter pressure systems and ice fog in Fairbanks, Alaska. Journal of Applied Meteorology. 1968;**7**:961-968

[4] Beran D, Hooke W, Clifford S. Acoustic echo-sounding techniques and their application to gravity-wave, turbulence, and stability studies. Boundary-Layer Meteorology. 1973;**4**:133-153

[5] Holmgren B, Spears L, Wilson C, Benson CS. Acoustic soundings of the Fairbanks temperature inversions. In: Weller G, Bowling SA, editors. Climate of the Arctic: Proceedings of the AAAS-AMS Conference, Fairbanks, Alaska. Geophysical Institute, University of Alaska; 1975, 1973. pp. 293-306

[6] Brown EH, Hall FF Jr. Advances in atmospheric acoustics. Reviews of Geophysics and Space Physics. 1978;**16**:47-110

[7] Fochesatto GJ, Mayfield JA, Gruber MA, Starkenburg D, Conner J. Occurrence of shallow cold flows in the winter atmospheric boundary layer of interior of Alaska. Meteorology and Atmospheric Physics. 2013. DOI: 10.1007/s00703-013-0274-4

[8] Clements WE, Archuleta JA, Hoard D. Mean structure of nocturnal drainage flow in a deep valley. Journal of Applied Meteorology. 1989;**28**:457-462

[9] Doran JC, Horst TW. Observations and models of simple nocturnal slope flows. Journal of the Atmospheric Sciences. 1983;**40**:708-717

[10] Benson CS. Ice Fog: Low Temperature Air Pollution, Defined with Fairbanks, Alaska as Type Locality. College, Alaska: University of Alaska Fairbanks, Geophysical Institute; 1965. p. 134

[11] Wendler G, Jayaweera K. Some measurements of the development of the surface inversion in Central Alaska during winter. Pure and Applied Geophysics. 1972;**99**:209-221

[12] Mölders N, Kramm G. A case study on wintertime inversions in interior Alaska with WRF. Atmospheric Research. 2010;**95**:314-332

[13] Benson CS. Ice fog. Weather. 1970;**25**:11-18

[14] Benson CS. Ice Fog: Low Temperature Air Pollution. CRREL Research Report 121; 1970

[15] Benson CS, Weller G. A Study of Low-Level Winds in the Vicinity of Fairbanks, Alaska. Report to Earth Resources Co. Geophysical Institute, University of Alaska; 1970

[16] Starkenburg D, Metzger S, Fochesatto GJ, Alfieri J, Gens R, Prakash A, et al. Assessment of de-spiking methods for turbulent flux computations in high latitude forest

canopies using sonic anemometers. Journal of Atmospheric and Oceanic Technology. 2016;**33**:2001-2013. DOI: 10.1175/JTECH-D-15-0154.1

[17] Kaimal JC, Finnigan JJ. Atmospheric Boundary Layer Flows: Their Structure and Measurement. Oxford University Press; 1994

[18] Wilczak J, Oncley S, Stage S. Sonic anemometer tilt correction algorithms. Boundary-Layer Meteorology. 2001;**99**:127-150

[19] Vickers D, Mahrt L. Quality control and flux sampling problems for tower and aircraft data. Journal of Atmospheric and Oceanic Technology. 1997;**14**:512-526

[20] Lee X, Massman W, Law B. Editors Handbook of Micrometeorology. A Guide for Surface Flux Measurements and Analysis. Dordrecht, Netherlands: Kluwer Academic Publishers; 2004

[21] Kleissl J, Gomez JSH, Hong SH, Hendrickx JMH, Rahn T, Defoor WL. Large aperture scintillometer intercomparison study. Boundary-Layer Meteorology. 2008;**128**:133-150

[22] De Bruin HAR, Meijninger WML, Smedman AS, Magnusson M. Displaced-beam small aperture scintillometer test. Part I: The Wintex data-set. Boundary-Layer Meteorology. 2002;**105**:129-148

[23] Gruber MA, Fochesatto GJ. A new sensitivity analysis and solution method for scintillometer measurements of area-average turbulent fluxes. Boundary-Layer Meteorology. 2013;**149**:65-83. DOI: 10.1007/s10546-013-9835-9

[24] Gruber MA, Fochesatto GJ, Hartogensis OK, Lysy M. Functional derivatives applied to error propagation of uncertainties in topography to large-aperture scintillometer-derived heat fluxes. Atmospheric Measurement Techniques. 2014;**7**:2361-2371. DOI: 10.5194/amt-7-2361-2014

[25] Fochesatto GJ. Methodology for determining multilayered temperature inversions. Atmospheric Measurement Techniques. 2015;**8**:2051-2060. DOI: 10.5194/amt-8-2051-2015

[26] Neff WD. An observational and numerical study of the atmospheric boundary layer overlying the east antarctic ice sheet. Ph.D. Thesis. Boulder, Colorado: University of Colorado; 1980

[27] Neff WD. Observations of complex terrain flows using acoustic sounders: Echo interpretation. Boundary-Layer Meteorology. 1988;**1988**(40):363-392

[28] Neff WD, King CW. Observations of complex-terrain flows using acoustic sounders–Experiments, topography, and winds. Boundary-Layer Meteorology. 1987;**40**:363-392

[29] Hootman BW, Blumen W. Analysis of nighttime drainage winds in boulder, Colorado during 1980. Monthly Weather Review. 1983;**111**:1052-1061

[30] Sakiyama SK. Drainage flow characteristics and inversion breakup in two Alberta Mountain valleys. Journal of Applied Meteorology. 1990;**29**:1015-1030

[31] Drobinski P, Brown RA, Flamant PH, Pelon J. Evidence of organized large Eddies by ground-based Doppler Lidar, sonic anemometer and sodar. Boundary-Layer Meteorology. 1998;**88**:343-361

[32] Mahrt L. The near-calm stable boundary layer. Boundary-Layer Meteorology. 2011; **140**:343-360

[33] Horst TW, Doran JC. Nocturnal drainage flow on simple slopes. Boundary-Layer Meteorology. 1986;**34**:263-286